

# Magnetism of ACFs and superfluidity of $^4\text{He}$ adsorbed in ACFs

Yoshiyuki Shibayama\*

College of Design and Manufacturing Technology, Muroran Institute of Technology, 27-1, Muroran, 050-8585, Japan

\*Corresponding author

DOI: 10.5185/amlett.2018.2129

www.vbripress.com/aml

## Abstract

Activated carbon fibers (ACFs) are a nanoporous form of carbon with huge specific surface areas caused by a three-dimensional random network of nanographites. Because of nano-size effects, non-bonding  $\pi$ -electron spins emerge on the nanographite. The nanographite random network produces many nanopores with a mean size of several nanometers and creates a host system for various guest molecules in ACFs. In order to investigate the magnetic properties of nanographite and the superfluidity of  $^4\text{He}$  restricted in nano-spaces, the magnetization of ACFs and superfluidity of  $^4\text{He}$  adsorbed in ACFs have been investigated. The magnetization shows an antiferromagnetic interaction between the non-bonding  $\pi$ -electron spins. Near the insulator-metal transition caused by heat treatment of ACFs, spin glass-like disordered magnetism observed. Up to an  $^4\text{He}$  coverage of  $22.6 \mu\text{mol}/\text{m}^2$ , no superfluidity is observed due to the strong van der Waals force between  $^4\text{He}$  and nanographite. Over  $23.7 \mu\text{mol}/\text{m}^2$   $^4\text{He}$  coverage, the superfluid transition is observed at approximately  $T_c \sim 500$  mK. Upon increasing the  $^4\text{He}$  coverage, the superfluid density increases, but no change in  $T_c$  is observed. These observations indicate that the thickness of superfluid films on nanographite is restricted by the slit type pore shape of ACFs. Copyright © 2018 VBRI Press.

**Keywords:** Activated carbon fibers (ACFs), nanographite, superfluid helium-4.

## Introduction

Activated carbon fibers (ACFs) are one form of disordered carbon materials. As their name implies, ACFs are a species of activated carbons having a fiber-like shape, with a length of several centimeters and a diameter of approximately  $10 \mu\text{m}$ . ACFs are remarkably unique in their extraordinarily large specific surface areas (SSAs). The SSAs range from  $1000$ - $3000 \text{ m}^2/\text{g}$ , which are much larger than those of ordinary activated carbon materials. In particular,  $3000 \text{ m}^2/\text{g}$  is a huge value compared with the theoretically calculated value for a single graphene sheet ( $2630 \text{ m}^2/\text{g}$ ). Because of their huge SSAs and enormous adsorptivity, ACFs have appeared in gas adsorption applications, electronic applications in double layer capacitors [1], and so on. Commercial ACFs are produced from ordinary carbon fibers through the activation process [2]. The carbon fibers are made mainly from the following different raw materials: pitch, phenol resin, polyacryl resin, and cellulose. The carbon fibers are activated in an oxidizing atmosphere, resulting in the formation of ACFs with nanoporous structures and huge SSAs. The as-grown ACFs are named after their precursors, i.e., pitch-based ACFs etc.

Although ACFs are industrial materials, their nanoporous structure with huge SSAs is so motivating from the viewpoint of applications, chemistry, carbon

science, and solid-state physics. The microscopic structures of ACFs are featured with the following two key words, *nanographite* (or *micrographite*) and *nanographite random network* [3]. The microscopic structure of the ACFs is shown in Fig. 1. Nanographite is a type of graphite crystallite, but its dimensions are much smaller than that of an ordinary graphite crystallite. In-plane crystallite size  $L_a$  and  $c$ -axis crystallite size  $L_c$  of the nanographite in as-grown ACFs are estimated at around  $3.0 \text{ nm}$  and  $1.1 \text{ nm}$  by Raman spectroscopy [4] and X-ray diffraction measurements [5], respectively. Because the crystallite size is considerably smaller, the nanographite is one nano-sized  $\pi$ -electron system with open edges around its periphery. From the viewpoint of the size of the  $\pi$ -electron system, the nanographite is similar to fullerenes or carbon nanotubes. The electronic structure of the nanographite, however, completely differs from those having closed  $\pi$ -electron structures. Theoretical studies [6-9] have predicted electronic states of nano-sized  $\pi$ -electron systems with open edges that depend crucially on their edge shape and size. Non-bonding  $\pi$ -electron spins, which never appear in regular bulk graphite with infinite  $\pi$ -electron planes or in closed  $\pi$ -electron systems of fullerenes and carbon nanotubes, emerge at the periphery of a nanographite.

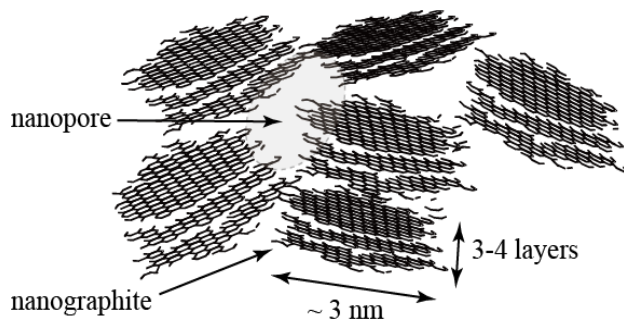


**Fig. 1.** Microscopic features of as-grown ACFs. Nanographite is composed of 3-4 layers of nanographene sheets. The three-dimensional disordered network in nanographites contains nanopores among nanographites.

The nanographite disordered network of ACFs produces a random network of nanopores with a mean size of several nanometers, leading to high porosity in ACFs. The existence of numerous nanopores has been confirmed by high resolution transmission electron microscopy (TEM) [10]. The random network of nanopores can accommodate the presence of a large number of various guest molecules. In the nanopores, the interaction between the adsorbed molecules with nanographite plays an important role. A previous investigation of iodine doped ACFs with  $^{129}\text{I}$  Mössbauer spectroscopy demonstrates the presence of charge transfer from nanographite to iodine [11], although no one has successfully synthesized iodine-graphite intercalation compounds ( $\text{I}_2$ -GICs) in bulk graphite [12]. Though  $^4\text{He}$  is noble gas,  $^4\text{He}$  shows extraordinarily huge condensation in the nanopores and the  $^4\text{He}$  density in the pore reaches approximately 1/10 of liquid  $^4\text{He}$ , even at room temperature [13].

Just as is known to occur in other carbon materials, the highly porous structure of ACFs is regularized by heat treatment [3], i.e., graphitization. Heat treatment up to about 1000 °C causes most of the functional groups to be pyrolyzed and stripped from the nanographite peripheries, but the nanographite itself is hardly influenced by heat treatment. Heat treatment at around 1200-1500 °C brings about a structural regularization of ACFs consisting of a three-dimensional disordered network of nanographites. Raman spectroscopy [4] and X-ray diffraction [5] indicate enhanced in-plane and *c*-axis crystallite sizes successively, which are caused by fusion of nanographites and three-dimensional ordering of the turbostratic structure. The three-dimensional ordering of the nanographite network depresses the nanoporous feature of ACFs. The SSAs start decreasing around a heat treatment temperature (HTT) of 1000 °C, resulting in nearly complete absence of the large SSAs up to around 2000 °C [3]. Eventually, in terms of both a nanographite and nanographite network, heat treatment greatly influences the structure of ACFs.

The highly turbostratic structure of ACFs brings about novel physical properties that are different from those of ordinary graphite. One of the unique physical properties is the electrical conductivity. As-grown ACFs exhibit conductivity around  $\sim 10^2$  S/m at room

temperature [14], which is considerably smaller than that of ordinary graphite [15]. Carrier transport in as-grown ACFs [16-18] is dominated by Coulomb gap variable-range hopping (CGVRH) conduction [19, 20]. This means that nanographite can be regarded as a nano-sized metallic domain. Thus, macroscopic carrier transport is subjected to a hopping process of carriers between metallic nanographite domains because of a lack of  $\pi$ -conjugated bridging between nanographites in the three-dimensional random network. The graphitization of ACFs influences CGVRH conduction in as-grown ACFs. Heat treatment around 1000-1300 °C induces a drastic changes in the electronic states in ACFs, i.e., an insulator-metal (I-M) transition [16-18]. Graphitization causes fusion of nanographites and three-dimensional ordering of the nanographite network, leading to the development of  $\pi$ -conjugated systems in nanographite ACFs. At last, the development of an infinite inter-nanographite percolation path network for carriers brings about an I-M transition.

From the viewpoint of highly porous features, ACFs are also interesting host materials to investigate  $^4\text{He}$  superfluidity confined in porous media. Liquid  $^4\text{He}$  is a typical quantum liquid, and it is phase-transferred into the superfluid phase at 2.17 K under saturated vapor pressure. The superfluidity of  $^4\text{He}$  adsorbed in nanoporous glass, which are  $\text{SiO}_2$ -based nanoporous media, is remarkably suppressed because of superfluid size effects in a restricted geometry [21, 22]. The nanoporous features of carbon ACFs offer two advantages to explore the superfluid size effects in a restricted geometry. One is that the pore size of ACFs can be easily controlled by graphitization. Unlike ACFs, the pore structure in porous glass is inflexible and pore sizes cannot be modified due to the rigid network of covalent Si-O bonds. Another advantage is that the pore walls of ACFs consist of nanographite, i.e., nano-sized graphite sheets. The accommodated  $^4\text{He}$  in ACFs is adsorbed on the surface of nanographites. Because superfluidity of  $^4\text{He}$  adsorbed on regular graphite has been investigated in detail [23], it is expected that we can discriminate superfluid size effects from interactions between the adsorbed  $^4\text{He}$  and the pore walls.

From the viewpoint of highly nanoporous carbon materials which consist of a three-dimensional random network of nanographites, we have investigated the electronic and magnetic properties of ACFs [11, 18, 24] and the behavior of molecules adsorbed in ACFs [11, 25]. The present paper is devoted to reviewing our studies on magnetic properties of ACFs in the vicinity of the I-M threshold [24] and on superfluidity of  $^4\text{He}$  adsorbed in ACFs [25].

## Experimental

### Materials

Commercial pitch-based ACFs type A15 were purchased from Osaka Gas Co. (Chuo-ku, Osaka, Japan). The SSAs of the as-purchased ACFs were estimated to be 2000  $\text{m}^2/\text{g}$  based on  $\text{N}_2$  adsorption measurements at 77 K.

Because ACFs are a highly porous carbon material, large amounts of various guest molecules are accommodated in the nanopores. Thus, before measurements the ACFs samples are vacuum heat-treated in order to remove any adsorbed molecules and are subsequently handled without exposing them to the atmosphere. The heat treatment conditions and sample handling after heat treatment are detailed in the following subsections.

### *Magnetic property measurements for ACFs*

Magnetic property measurements for ACFs are carried out with a SQUID magnetometer Model MPMS5 manufactured by Quantum Design Inc. (San Diego, CA, USA) at temperatures in the 2-380 K range and with magnetic fields at 1 T.

A bundle of approximately 15 mg as-purchased ACFs was wadded in the center of a quartz tube with outer and inner diameters of 7.0 mm and 5.5 mm, respectively, with an approximately 30 cm long closed end. In order to remove adsorbed molecules, especially paramagnetic oxygen, the sample was heat-treated at 800 °C and at  $1 \times 10^{-4}$  Pa for 1 hour in the quartz tube. After vacuum heat treatment, the sample was vacuum-sealed in the quartz tube. The heat-treated sample in the quartz tube, labelled HTT800, was set on the SQUID magnetometer, and magnetization measurements were carried out. After gathering measurements, the HTT800 sample was re-heat-treated for 15 min at 900 °C with the sample kept in the vacuum-sealed quartz tube. After re-heat treatment, magnetization measurements for the HTT900 sample were performed. Similar procedures were performed successively up to 1500 °C. Finally, heat treatment at 1500 °C for 1 hour was performed. The sample, labelled HTT 1500 (1h), was the most intense heat treatment performed in the series of studies.

### *Torsional oscillator studies for superfluid <sup>4</sup>He adsorbed in ACFs*

Superfluidity of <sup>4</sup>He adsorbed in ACFs was studied with a torsional oscillator method [22, 26] down to 20 mK with a commercial <sup>3</sup>He/<sup>4</sup>He dilution refrigerator manufactured by CryoConcept Co. (Courtaboeuf, France). The homemade torsional oscillator consists of a BeCu alloy sample cell containing the ACFs sample and a hollow torsion rod made of BeCu alloy acting as a He filling line. The resonance frequency  $f$  of torsional oscillations is

$$f = \frac{1}{2\pi} \sqrt{\frac{\kappa}{I_0 + I_{\text{He}}}},$$

where  $\kappa$ ,  $I_0$  and  $I_{\text{He}}$  are the torsional spring constant of the torsion rod, the moment of inertia of the sample cell containing the porous host sample, and the moment of inertia of the <sup>4</sup>He admitted into the sample cell, respectively. The resonance frequency and the quality factor  $Q$  of the employed oscillator are approximately 683.115 Hz and  $6.2 \times 10^5$  at 20 mK, respectively. In the

torsional oscillator method, superfluidity is detected by measuring changes in the resonance frequency, because the superfluid component in the sample cell does not contribute to  $I_{\text{He}}$ . Before the introduction of <sup>4</sup>He, the resonance frequency was measured as a function of temperature. The temperature dependence of the resonance frequency  $f(T)$  is only caused by changes in  $\kappa$  due to temperature changes in the torsion rod. After measurement, a certain amount of <sup>4</sup>He was fed into the sample cell at 2 K using a room-temperature gas handling system. After admission, the sample cell was annealed at 10 K and then cooled down slowly in order to ensure that <sup>4</sup>He adsorption was uniform over the ACFs sample. Then the resonance frequency was again measured as a function of temperature. Below the superfluid transition temperature  $T_c$ , a finite frequency shift  $\Delta f(T)$  was observed, which is proportional to the superfluid density. The superfluidity of <sup>4</sup>He confined in the ACFs sample was investigated for a wide range of <sup>4</sup>He densities. When the amount of <sup>4</sup>He introduced into the sample cell is not sufficient to fill the pores of the ACFs sample, <sup>4</sup>He formed adsorbed films on the pore walls. The coverage of <sup>4</sup>He adsorbed on the pore walls was controlled by the amount of <sup>4</sup>He introduced into the sample cell. Successive introduction of <sup>4</sup>He eventually fills the nanopores with liquid <sup>4</sup>He, and the gas and bulk liquid <sup>4</sup>He coexist in the open space of the cell at saturated vapor pressures.

An ACFs sample is prepared as follows. A bundle of 87.11 mg as-purchased ACFs was stuffed into the sample cell. The bundle was pressed with a screw cap made of brass in order to hold the ACFs tightly in the cell. In order to remove adsorbed molecules, vacuum heat-treatment of the ACFs sample was performed at 150 °C for 1 hour at  $1 \times 10^{-4}$  Pa through the <sup>4</sup>He filling line.

## Results and discussion

### *Magnetic properties of ACFs around insulator-metal transition*

The temperature dependence of magnetization  $M$  per 1 g for HTT800-1500(1h) ACFs samples under 1 T is shown in Fig. 2. Magnetization of the ACFs samples heat-treated under 1100 °C follows the Curie-Weiss law over the entire temperature range investigated. This means that the samples have localized spins. For the sample heat-treated at 1200 °C, where graphitization causes I-M transition to ACFs [16-18], the magnetization deviates from the Curie-Weiss law below approximately 20 K and shows a cusp around 7 K. The magnitude of the cusp was depressed when the heat treatment temperature increased. The cusp strongly depends on the cooling processes. Fig. 3 shows field-cooling effects on the magnetization for HTT800 and HTT1100 ACFs samples, where the samples were prepared independently of those shown in Fig. 2. The measurements were carried out at 1 T in heating runs after cooling from room temperature to 2 K with zero-field-cooling and 1 T field-cooling. Magnetization of the HTT800 sample following the

Curie-Weiss law is independent of the cooling processes. This is typical Curie-Weiss behavior and originates from ordinary localized electron magnetism. The cusp of magnetization in the HTT1100 sample, however, is strongly enhanced by field-cooling. The features are reminiscent of a spin glass state in amorphous magnets [27].

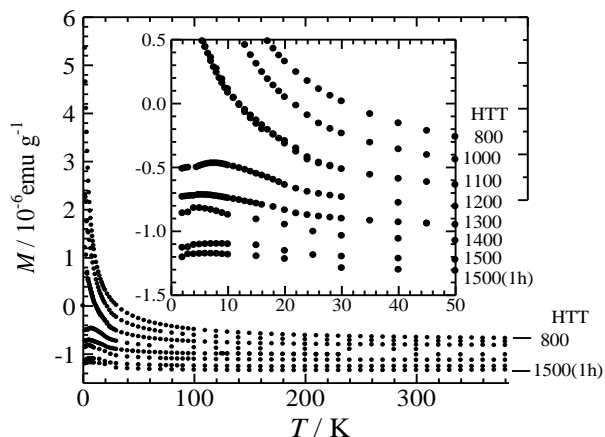


**Fig. 2.** Temperature dependence of magnetization  $M$  under 1 T for ACFs heat-treated up to  $\text{HTT} = 1500^\circ\text{C}$ . Detailed behavior at low temperatures is shown in the inset.

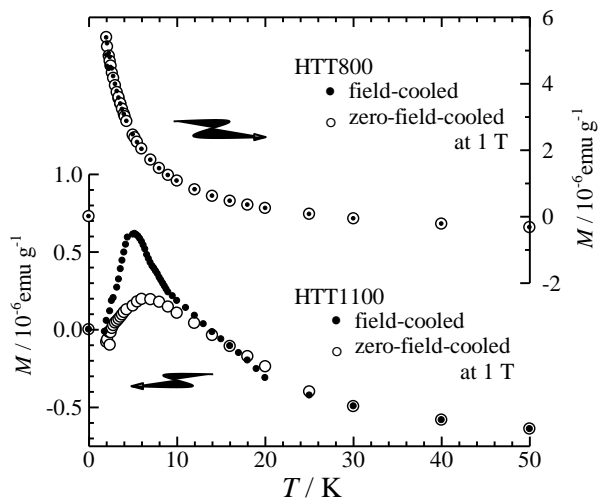


**Fig. 3.** Field cooling effect of magnetization  $M$  under 1 T for the HTT800 and HTT1100 ACFs samples.

In order to estimate the spin density and the magnitude of the interaction among the spins, a least squares fit is performed based on the assumption that the observed magnetic susceptibility  $\chi = M/H$  is the sum of the Curie-Weiss term  $C/(T - \theta)$  and the temperature-independent term  $\chi_0$ , where  $C$  and  $\theta$  are the Curie constant per 1 g ACFs sample and the Weiss temperature, respectively. Here, spin angular momentum  $s = 1/2$  and  $g$ -value  $g = 2$  are taken because the observed spins originate from carbon materials. In **Fig. 4**, fitting results are shown, where  $N_{\text{spin}}$  and  $n_{\text{spin}}$  are the number of spins per 1 g ACFs sample and per nanographite, respectively.  $n_{\text{spin}}$  was estimated using the nanographite

in-plane size [18]. Heat treatment diminishes the spin density  $N_{\text{spin}}$  from  $4.2 \times 10^{19} \text{ g}^{-1}$  (HTT800 sample) to  $0.39 \times 10^{19} \text{ g}^{-1}$  (HTT1500(1h) sample). The number of spins per nanographite  $n_{\text{spin}}$ , in contrast with the large decrease in spin density, ranges from 1 to 0.5 and is relatively unaffected by heat treatment. The discrepancy is caused by the growth of the nanographite in-plane size due to heat treatment. In short, each nanographite has  $\sim 1$  spin irrespective of the nanographite in-plane size. This gives important information on the magnetism of the nanographite sample. In general, the localized spins observed in disordered carbon materials consisting of  $sp^2$  and  $sp^3$  C-C bonds network have been considered to originate from  $\sigma$ -dangling bonds [28]. In contrast, the nanographites generating ACFs are composed of well-characterized condensed polycyclic aromatic rings with few  $sp^3$ -bonds bridging nanographite [3-5]. Moreover, in relation to the appearance of novel magnetism in nanographites, theoretical studies predict the presence of non-bonding  $\pi$ -electron edge states, which are localized on the peripheral carbon atoms that form zigzag edges, even if these carbon atoms are terminated by foreign atoms like hydrogen [7-9]. These theoretical predictions have been reinforced by experimental observations of novel edge-state-based magnetism in graphite nanoparticles prepared by heat treatment of diamond nanoparticles [29]. Hence, the spins observed in this work are considered to originate from the non-bonding edge states of  $\pi$ -electrons.

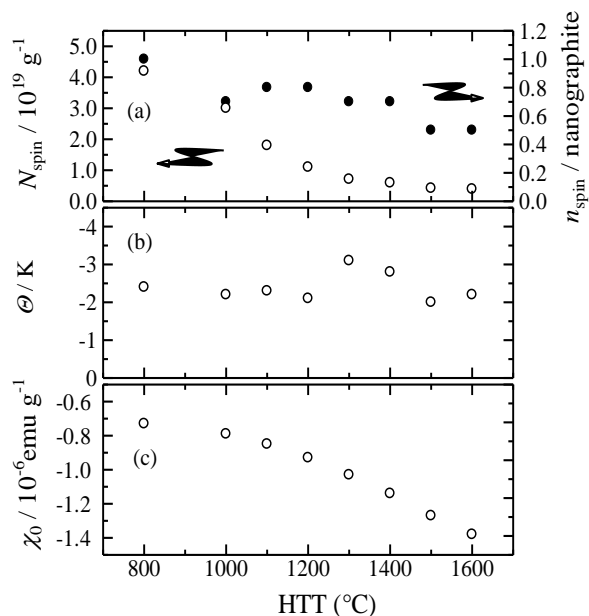


**Fig. 4.** (a) Spin density  $N_{\text{spin}}$  per 1 g ACFs sample (open circles) and number of spins per one nanographite  $n_{\text{spin}}$  (solid circles), (b) Weiss temperature  $\theta$ , and (c) temperature-independent  $\chi_0$  for all the samples in **Fig. 2**. The data for HTT1500(1h) sample is positioned at  $\text{HTT} = 1600^\circ\text{C}$ .

The constant term  $\chi_0$  is negative for all ACFs samples and the magnitude of the term is enhanced by the heat treatment. The constant term  $\chi_0$  for graphite and carbon materials originates from Pascal and Landau

diamagnetism [18]. Because the Pascal diamagnetism of graphite contains a contribution from inner shell electrons in carbon atoms, the magnitude of the Pascal diamagnetism is independent of the heat treatment. By contrast, the Landau diamagnetism originates from itinerant  $\pi$ -electrons, and enhanced diamagnetism in the ACFs heat-treated up to 2800 °C is well-explained by an increase in Landau diamagnetism [18]. Hence, the present enhancement of  $\chi_0$  is also caused by the development of Landau diamagnetism. This demonstrates the itinerant  $\pi$ -electron system of the nanographite network due to heat treatment at higher temperatures.

The Weiss temperature has similar negative values in the -2 to -3 K range, irrespective of the sample heat treatment. The negative Weiss temperature demonstrates the presence of antiferromagnetic interactions among the observed localized non-bonding  $\pi$ -electrons at the edge states. Since each nanographite has around 1 spin, the mean distance between spins is in the same range as the nanographite in-plane size,  $L_a \sim 3\text{-}5$  nm [18]. This distance is too long for direct exchange interactions between spins. Thus, the exchange interaction between the localized non-bonding  $\pi$ -electrons is considered to be mediated by  $\pi$ -electrons on the nanographites. This picture is similar to the  $s$ - $d$  interaction in transition metal magnets. The considerably enhanced electronic specific heat with large magnetic field dependence in disordered carbon materials [30] supports evidence for the exchange interaction mediated by  $\pi$ -electrons.

The appearance of the cusp in the magnetization and the cusp enhancement by field-cooling of the ACFs samples in the vicinity of the I-M threshold also support the scenario that  $\pi$ -electrons mediate the exchange interaction between the localized non-bonding  $\pi$ -electrons. The ACFs samples in the insulator region, which are heat-treated at low temperatures, have no infinite exchange interaction network mediated by  $\pi$ -electrons. Therefore, the magnetization shows typical Curie-Weiss behavior over the whole temperature range investigated. Graphitization by heat treatment suppresses the turbostratic structure of ACFs, resulting in an I-M transition at heat treatment temperatures of 1100-1200 °C. The I-M transition demonstrates the development of an infinite inter-nanographite random percolation path network for  $\pi$ -electron carriers. Through the random percolation path network, the itinerant  $\pi$ -electrons can mediate the antiferromagnetic interaction between localized non-bonding  $\pi$ -electrons at the edge states across the ACFs. Eventually, disordered magnetism like a spin-glass behavior appears in the ACFs samples near the vicinity of the I-M threshold. Increasing the heat treatment temperature promotes graphitization of ACFs. As a result, the randomness of the inter-nanographite percolation path network is depressed. This leads to the disappearance of the cusp caused by disordered magnetism.

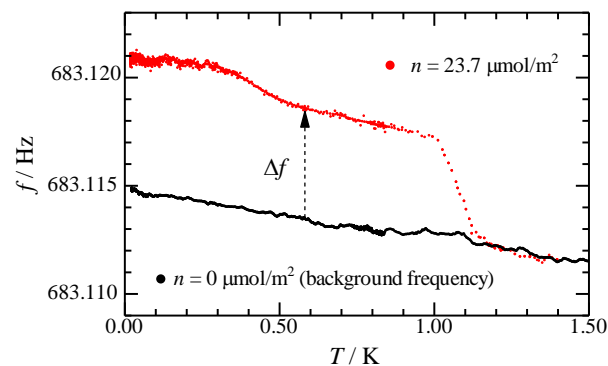


**Fig. 5.** Temperature dependence of the torsional oscillator resonance frequency  $f$ , where the black and red circles show results for  $^4\text{He}$  coverage  $n = 0 \mu\text{mol/m}^2$  (background frequency) and  $23.7 \mu\text{mol/m}^2$ , respectively. The red data points are shifted by  $+0.3072$  Hz in order to clarify the response caused by the adsorbed  $^4\text{He}$ . The change in  $f$  from background is the frequency shift  $\Delta f$  due to mass decoupling of the adsorbed  $^4\text{He}$ .

### Superfluidity of $^4\text{He}$ adsorbed in ACFs

Typical results from the torsional oscillator study for superfluidity are shown in Fig. 5. The black circles indicate the temperature dependence of the resonance frequency of the torsional oscillator containing the ACFs sample before  $^4\text{He}$  adsorption. The resonance frequency slightly increases with decreasing of the temperature because of the temperature change in the torsional spring constant of the torsion rod. Red circles indicate the temperature dependence of the resonance frequency after admission of  $^4\text{He}$ , where the  $^4\text{He}$  coverage  $n$  is  $23.7 \mu\text{mol/m}^2$ . Here, the observed frequencies are shifted by  $+0.3072$  Hz in order to clarify the response due to the adsorbed  $^4\text{He}$ , because the adsorbed  $^4\text{He}$  decreases the resonance frequency by its moment of inertia. At 550 mK and 1.1 K, upturns in the resonance frequency are observed. The frequency shift from the background  $\Delta f(T)$  indicates mass decoupling of the adsorbed  $^4\text{He}$  in the nanopores of the ACFs sample.

In order to clarify the frequency shift  $\Delta f(T)$  from the background,  $\Delta f(T)$  is plotted as a function of temperature for 7.1, 20.9, 21.8, 22.6, 23.7, 29.3, 38.3, 42.4, and  $51.1 \mu\text{mol/m}^2$   $^4\text{He}$  coverage in Fig. 6a. Up to a coverage  $n = 22.6 \mu\text{mol/m}^2$ , no frequency shift is observed at the investigated temperatures, i.e., no superfluidity is observed. This indicates that the strong van der Waals attraction between the accommodated  $^4\text{He}$  in the nanopores and the nanopore walls consisting of nanographite surfaces suppresses the superfluid transition of the adsorbed  $^4\text{He}$ . At a coverage of  $23.7 \mu\text{mol/m}^2$ , finite frequency shift is observed at 550 mK and 1.1 K. Over  $29.3 \mu\text{mol/m}^2$ , the frequency shift due to superfluidity of bulk  $^4\text{He}$  is observed at 2.2 K. The bulk  $^4\text{He}$  is present in the open space in the sample cell. The frequency shift originates as the bulk superfluid  $^4\text{He}$  enhances with increased coverage, while the frequency shifts at lower temperatures are almost independent of coverage. At  $51.1 \mu\text{mol/m}^2$  these shifts disappear because of the large contribution of bulk superfluid  $^4\text{He}$ . Here, anomalies which appear at 1-2 K

for 23.7, 38.3, and 42.4  $\mu\text{mol}/\text{m}^2$  samples are associated with desorption of  $^4\text{He}$  and are not caused by superfluidity.

The temperature dependence of the frequency shift below 1.4 K is replotted in **Fig. 6b**. Here, in order to clarify the frequency shift other than that caused by bulk superfluid  $^4\text{He}$ , the  $\Delta f(T)$  is shifted so as to collapse onto a single curve at 600-800 mK. Two characteristic onset temperatures of 550 mK and 1.1 K are independent of  $^4\text{He}$  coverage. The magnitude of the frequency shift at 550 mK increases with increased coverage up to 38.3  $\mu\text{mol}/\text{m}^2$ , and then turns to a decrease. By contrast, the size of the frequency shift at 1.1 K is independent of  $^4\text{He}$  coverage. These features are not the usual superfluidity response of  $^4\text{He}$  confined in nanoporous glass [21, 22].

Now, we discuss the origin of the frequency shift observed at 23.7  $\mu\text{mol}/\text{m}^2$  at 550 mK. The phase diagram of  $^4\text{He}$  adsorbed on ordinary graphite was investigated in detail by P. A. Crowell and J. D. Reppy [23]. The growth of  $^4\text{He}$  films on the basal plane of graphite occurs in a layer-by-layer fashion, and no superfluidity is observed in the first layer of  $^4\text{He}$  films because of the van der Waals attraction between  $^4\text{He}$  and the graphite surface. The second layer begins to fill  $n = 19.9 \mu\text{mol}/\text{m}^2$  (12.0  $^4\text{He}$  atoms/ $\text{nm}^2$ ), and the third and the fourth layers begin at 33.9  $\mu\text{mol}/\text{m}^2$  and 47  $\mu\text{mol}/\text{m}^2$ , respectively. At around 300 mK, they first observe superfluidity in  $^4\text{He}$  films on graphite at 28.3  $\mu\text{mol}/\text{m}^2$  coverage, which is the upper half of the second layer. The superfluid response becomes large with increased coverage, and again disappears near the completion of the second layer. In the third layer, superfluidity is first observed at 36.0  $\mu\text{mol}/\text{m}^2$ , and both the superfluid response and transition temperature increase with increased coverage. In this work, the present coverage of 23.7  $\mu\text{mol}/\text{m}^2$  corresponds to the upper half of the second layer region on the assumption that  $^4\text{He}$  layers adsorbed on the nanographite surfaces grow in the same fashion as those on the basal plane of graphite. Therefore the finite frequency shift observed at 23.7  $\mu\text{mol}/\text{m}^2$  at 550 mK originates from the superfluidity of the second  $^4\text{He}$  layer adsorbed on the nanographite surfaces.

The frequency shift observed at 550 mK due to  $^4\text{He}$  superfluidity accommodated in ACF nanopores shows a curious feature. In short, the superfluid transition temperature is independent of  $^4\text{He}$  coverage. In the case of both superfluid  $^4\text{He}$  films adsorbed on regular graphite [23] and superfluidity of  $^4\text{He}$  restricted in nanoporous glass [21, 22], the superfluid transition temperature increases with increased  $^4\text{He}$  coverage. The curious feature is explained by the structural model of ACF nanopores. According to N. Setoyama *et al.* [31], the ACF nanopore geometry is not cylindrical but is instead slit-type, where the clearance of the slit is in the 0.7 - 1 nm range. Assuming that the  $^4\text{He}$  hardcore size is 0.35 nm [22], the slit clearance corresponds to 2-3 atomic layers of  $^4\text{He}$ . Because adsorbed  $^4\text{He}$  films grow on both sides of the pore wall, approximately 1.5

adsorption layers on one side of the pore wall fills the pores, and excess  $^4\text{He}$  is not accommodated in the pores. This scenario explains the present experimental results. At a coverage of 23.7  $\mu\text{mol}/\text{m}^2$ , which corresponds to the upper half of the second layer, only superfluidity in the nanopore is observed. The nanopore is almost filled at a coverage of approximately 1.5 atomic layers. Excess  $^4\text{He}$  in the open space of the cell is phase-transferred into the superfluid phase at 2.2 K.

Although the frequency shift at 1.1 K, which is independent of  $^4\text{He}$  coverage, also seems to be caused by superfluid transition, the temperature of 1.1 K is too high for superfluidity of the second  $^4\text{He}$  layer [23]. Because the layer-by-layer growth of the  $^4\text{He}$  films on nanographite is prevented by the slit type pore shape, the  $^4\text{He}$  films do not form third layers. A possible origin of the frequency shift is slippage of the nonsuperfluid  $^4\text{He}$  films [32]. The study of  $^4\text{He}$  films on graphite using quartz-crystal microbalance (QCM) techniques, where the resonance frequency of QCM is 5 MHz and is much higher than that of the present torsional oscillator, demonstrates slippage of the second adsorbed  $^4\text{He}$  layer at temperatures ranging from 1 to 2 K. In the QCM study, the onset temperature of the slippage decreases with increased  $^4\text{He}$  coverage, in contrast with the present results. The difference between the torsional oscillator and the QCM experiments may arise due to the different resonance frequencies.

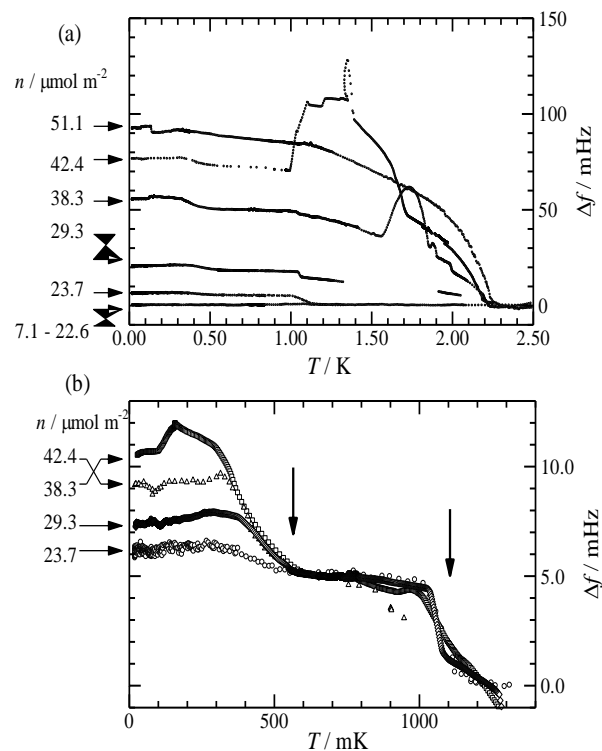


**Fig. 6.** (a) Frequency shift  $\Delta f(T)$  for  $n = 7.1, 20.9, 21.8, 22.6, 23.7, 29.3, 38.3, 42.4,$  and  $51.1 \mu\text{mol}/\text{m}^2$   $^4\text{He}$  coverage. No frequency shift is observed up to  $22.6 \mu\text{mol}/\text{m}^2$ . (b)  $\Delta f(T)$  for various  $^4\text{He}$  coverage measurements. In order to clarify the behavior of  $\Delta f(T)$ , the data collapse onto a single curve at 600-800 mK. The ordinate is valid for the  $23.7 \mu\text{mol}/\text{m}^2$  sample data. The arrows indicate the onset of anomalies in  $\Delta f(T)$ .

## Conclusion

Magnetization of heat-treated ACFs and superfluidity of  $^4\text{He}$  accommodated in ACFs were explored in order to investigate the magnetic properties of nanographite and superfluidity of  $^4\text{He}$  restricted in nanoporous carbons composed of a nanographite random network. Novel magnetism caused by localized non-bonding  $\pi$ -electrons at the edge states is observed. Disordered magnetism similar to a spin glass state was observed in the vicinity of the insulator-metal threshold. At  $^4\text{He}$  coverage of  $23.7 \mu\text{mol}/\text{m}^2$ , superfluidity of  $^4\text{He}$  adsorbed in ACFs was observed at 550 mK. The superfluidity is almost independent of the  $^4\text{He}$  coverage because the slit-type pore shape restricts the growth of  $^4\text{He}$  films in the ACF nanopores.

## Acknowledgements

The author thanks Prof. T. Enoki, Prof. H. Sato, Prof. M. Fujita, and Prof. Sugihara for helpful discussion on the electronic state of nanographite, and Prof. K. Shirahama and Prof. M. Suzuki for helpful discussion of superfluidity in a restricted geometry. This work is partly supported by KAKENHI from JSPS.

## Author's contributions

The author has no competing financial interests.

## References

- Endo, M.; Okada, Y.; Nakamura, H.; *Synth. Met.*, **1989**, *34*, 739.  
DOI: [10.1016/0379-6779\(89\)90468-2](https://doi.org/10.1016/0379-6779(89)90468-2)
- Pandolfo, A. G.; Hollenkamp, A. F.; *J. Power Sources*, **2006**, *157*, 11.  
DOI: [10.1016/j.jpowsour.2006.02.065](https://doi.org/10.1016/j.jpowsour.2006.02.065)
- Dresselhaus, M. S.; Fung, A. W. P.; Rao, A. M.; di Vittorio, S. L.; Kuriyama, K.; Dresselhaus, G.; Endo, M.; *Carbon*, **1992**, *30*, 1065.  
DOI: [10.1016/0008-6223\(92\)90138-M](https://doi.org/10.1016/0008-6223(92)90138-M)
- Rao, A. M.; Fung, A. W. P.; Dresselhaus, M. S.; Dresselhaus, G.; Endo, M.; *J. Mater.*, **1992**, *7*, 1788.  
DOI: [0.1557/JMR.1992.1788](https://doi.org/0.1557/JMR.1992.1788)
- Kuriyama, K.; Dresselhaus, M. S.; *J. Mater. Res.*, **1991**, *6*, 1040.  
DOI: [10.1557/JMR.1991.1040](https://doi.org/10.1557/JMR.1991.1040)
- Yoshizawa, K.; Okahara, K.; Sato, T.; Tanaka, K.; Yamabe, T.; *Carbon*, **1994**, *32*, 1517.  
DOI: [10.1016/0008-6223\(94\)90147-3](https://doi.org/10.1016/0008-6223(94)90147-3)
- Fujita, M.; Wakabayashi, K.; Nakada, K.; Kusakabe, K.; *J. Phys. Soc. Jpn.*, **1996**, *65*, 1920.  
DOI: [10.1143/JPSJ.65.1920](https://doi.org/10.1143/JPSJ.65.1920)
- Fujita, M.; Igami, M.; Nakada, K.; *J. Phys. Soc. Jpn.*, **1997**, *66*, 1864.  
DOI: [10.1143/JPSJ.66.1864](https://doi.org/10.1143/JPSJ.66.1864)
- Wakabayashi, K.; Fujita, M.; Ajiki, H.; Sigrist, M.; *Phys. Rev. B*, **1999**, *59*, 8271.  
DOI: [10.1103/PhysRevB.59.8271](https://doi.org/10.1103/PhysRevB.59.8271)
- Oshida, K.; Endo, M.; Nakajima, T.; di Vittorio, S. L.; Dresselhaus, M. S.; Dresselhaus, G.; *J. Mater. Res.*, **1993**, *8*, 512.  
DOI: [10.1557/JMR.1993.0512](https://doi.org/10.1557/JMR.1993.0512)
- Shibayama, Y.; Sato, H.; Enoki, T.; Seto, M.; Kobayashi, Y.; Maeda, Y.; Endo, M.; *Mol. Cryst. Liq. Cryst.* **2000**, *340*, 301.  
DOI: [10.1080/10587250008025483](https://doi.org/10.1080/10587250008025483)
- Dresselhaus, M. S.; Dresselhaus, G.; *Adv. Phys.*, **1981**, *30*, 139.  
DOI: [10.1080/00018738100101367](https://doi.org/10.1080/00018738100101367)
- Enoki, T.; Kobayashi, N.; Nakayama, A.; Suzuki, K.; Ishii, C.; Kaneko, K.; Hosokoshi, Y.; Kinoshita, M.; Endo, M.; Shindo, N.; *Mat. Res. Soc. Symp. Proc.*, **1994**, *349*, 73.  
DOI: [10.1557/PROC-349-73](https://doi.org/10.1557/PROC-349-73)
- di Vittorio, S. L.; Dresselhaus, M. S.; Endo, M.; Issi, J. P.; Piraux, L.; Bayot, V.; *J. Mater. Res.*, **1991**, *6*, 778.  
DOI: [10.1557/JMR.1991.0778](https://doi.org/10.1557/JMR.1991.0778)
- Dresselhaus, M. S.; Dresselhaus, G.; Sugihara, K.; Spain, I. L.; Goldberg, H. A.; *Graphite Fibers and Filaments*; Springer-Verlag, Germany, 1988.  
DOI: [10.1007/978-3-642-83379-3](https://doi.org/10.1007/978-3-642-83379-3)
- Fung, A. W. P.; Dresselhaus, M. S.; Endo, M.; *Phys. Rev. B*, **1993**, *48*, 14953.  
DOI: [10.1103/PhysRevB.48.14953](https://doi.org/10.1103/PhysRevB.48.14953)
- Fung, A. W. P.; Wang, Z. H.; Dresselhaus, M. S.; Dresselhaus, G.; Pekala, R. W.; Endo, M.; *Phys. Rev. B*, **1994**, *49*, 17325.  
DOI: [10.1103/PhysRevB.49.17325](https://doi.org/10.1103/PhysRevB.49.17325)
- Shibayama, Y.; Sato, H.; Enoki, T.; Bi, X. X.; Dresselhaus, M. S.; Endo, M.; *J. Phys. Soc. Jpn.*, **2000**, *69*, 754.  
DOI: [10.1143/JPSJ.69.754](https://doi.org/10.1143/JPSJ.69.754)
- Efros, A. L.; Shklovskii, B. I.; *J. Phys. C: Solid State Phys.*, **1975**, *8*, L49.  
DOI: [10.1088/0022-3719/8/4/003](https://doi.org/10.1088/0022-3719/8/4/003)
- Efros, A. L.; *J. Phys.: C Solid State Phys.*, **1976**, *9*, 2021.  
DOI: [10.1088/0022-3719/9/11/012](https://doi.org/10.1088/0022-3719/9/11/012)
- Shirahama, K.; Kubota, M.; Ogawa, S.; Wada, N.; Watanabe, T.; *Phys. Rev. Lett.*, **1990**, *64*, 1541.  
DOI: [10.1103/PhysRevLett.64.1541](https://doi.org/10.1103/PhysRevLett.64.1541)
- Yamamoto, K.; Nakashima, H.; Shibayama, Y.; Shirahama, K.; *Phys. Rev. Lett.*, **2004**, *93*, 075302.  
DOI: [10.1103/PhysRevLett.93.075302](https://doi.org/10.1103/PhysRevLett.93.075302)
- Crowell, P. A.; Reppy, J. D.; *Phys. Rev. B*, **1996**, *53*, 2701.  
DOI: [10.1103/PhysRevB.53.2701](https://doi.org/10.1103/PhysRevB.53.2701)
- Shibayama, Y.; Sato, H.; Enoki, T.; Endo, M.; *Phys. Rev. Lett.*, **2000**, *84*, 1744.  
DOI: [10.1103/PhysRevLett.84.1744](https://doi.org/10.1103/PhysRevLett.84.1744)
- Shibayama, Y.; Shirahama, K.; *J. Low Temp. Phys.*, **2007**, *148*, 809.  
DOI: [10.1007/s10909-007-9440-8](https://doi.org/10.1007/s10909-007-9440-8)
- Shibayama, Y.; Shirahama, K.; *J. Phys. Soc. Jpn.*, **2011**, *80*, 084604.  
DOI: [10.1143/JPSJ.80.084604](https://doi.org/10.1143/JPSJ.80.084604)
- Mezard, M.; Raris, G.; Virasoro, M. A.; *Spin Glass Theory and Beyond*; World Scientific, USA, **1987**.  
DOI: [10.1142/9789812799371\\_0007](https://doi.org/10.1142/9789812799371_0007)
- Lewis, I. C.; Singer, L. S.; *Chemistry and Physics of Carbon Vol. 17*, Marcel Dekker Inc., USA, **1981**.
- Anderson, O. E.; Prasad, B. L. V.; Sato, H.; Enoki, T.; Hishiyama, Y.; Kaburagi, Y.; Yoshikawa, M.; Bandow, S.; *Phys. Rev. B*, **1998**, *58*, 16387.  
DOI: [10.1103/PhysRevB.58.16387](https://doi.org/10.1103/PhysRevB.58.16387)
- Mrozowski, S.; *J. Low Temp. Phys.*, **1979**, *35*, 231.  
DOI: [10.1007/BF00](https://doi.org/10.1007/BF00)
- Setoyama, N.; Ruike, M.; Kasu, T.; Suzuki, T.; Kaneko, K.; *Langmuir*, **1993**, *9*, 2612.  
DOI: [10.1021/la00034a021](https://doi.org/10.1021/la00034a021)
- Hosomi, N.; Tanabe, A.; Suzuki, M.; Hieda, M.; *Phys. Rev. B*, **2007**, *75*, 064513.  
DOI: [10.1103/PhysRevB.75.064513](https://doi.org/10.1103/PhysRevB.75.064513)